Identifying Active Regions of Finite-Wing Transonic Buffet using Resolvent Method

Jelle Houtman*, U S Vevek† and Sebastian Timme‡
University of Liverpool, Liverpool, L69 3GH, United Kingdom

Shock-wave/boundary-layer interaction on wings can result first in self-sustained flow unsteadiness called shock buffet and eventually in a structural response called buffeting. While it is an important aspect of wing design and aircraft certification, particularly for modern transonic air transport, neither are all of the underlying physics thoroughly understood nor does a typical industrial analysis make use of the latest simulation capability in unsteady aerodynamics. Previously, resolvent studies have been carried out for shock buffet on aerofoils, but only recently has this been done for three-dimensional, practical aircraft [1]. Herein, this study is expanded upon by using the windowed resolvent method to further investigate the origin of shock buffet. A novel windowed inexact subspace iterative resolvent algorithm, necessary for cases of this size, is introduced and scrutinised in an industrial computational fluid dynamics solver. Essentially, the truncated singular value decomposition of the discretised resolvent operator is returned, giving the optimal energy gain plus forcing and response modes of the system at chosen forcing frequencies. Additionally, it allows the filtering of selected regions of the computational domain (and/or chosen equations). The test cases are a two-dimensional cylinder for verification purposes and the NASA Common Research Model, for which we previously performed both triglobal stability and resolvent analyses. We aim to contribute to the question on the origin of shock buffet on aircraft wings and control thereof.

I. Introduction

Within the field of fluid mechanics, the ability to identify modal features in the flow that can be linked to real-life flow phenomena can be very useful. This helps design, for instance, aeroplanes, by preventing unwanted behaviour such as flutter, limit cycle oscillations and shock buffet, to name a few. The latter, shock buffet, is described by self-excited large-scale oscillations over aeroplane wings at transonic conditions, caused by shock-wave/boundary-layer interactions. Although it has been known since the 1960s, a complete understanding has not yet been accomplished, and it is therefore an intensively studied topic. One of the earliest explanations was given in [2], who proposed a feedback loop as the driving mechanism. Additionally, experimental and numerical work has identified outboard-propagating 'buffet cells', which are a characteristic feature of shock buffet on wings. The discovery of an unstable global mode in [3] was a catalyst for increasing interest in the subject. Similar studies were conducted on infinite wings [4–6] and recently global instabilities linked to shock buffet have been found on practical finite-wing aircraft [7, 8]. These studies were extended to investigate the role of fluid-structure interaction [9, 10]. Additionally, and important for the current study, the aerofoil work in [11] utilised selective frequency damping alongside global stability analysis. Among other findings, it was concluded that models for shock buffet dynamics that rely on circumventing the supersonic zone do not describe a mechanism at the core of shock buffet. Instead, they more likely are a consequence of the phenomenon.

Complementary to global stability analysis, resolvent analysis can further aid in investigating interesting modal behaviour. Resolvent analysis is concerned with the properties of the resolvent operator, which arises from an input-output formulation, resulting in an (input) forcing and (output) response mode at a specified forcing frequency. The properties of this operator can reveal pseudo-resonance due to non-normality of the Jacobian operator of the (Reynolds-averaged) Navier–Stokes equations. Resolvent analysis has been performed on a myriad of fundamental flow configurations, such as Poiseuille and turbulent shear flows [12–14]. Relevant to our work, such a study was also conducted for a two-dimensional aerofoil encountering shock buffet in [15]. Besides uncovering the now well-known aerofoil buffet dynamics, resolvent analysis also identified a second resonance linked to a wake mode. Equivalent observations were

*PhD Student, School of Engineering, jelle.houtman@liverpool.ac.uk.
†Postdoctoral Research Associate, School of Engineering.
‡Reader, School of Engineering, sebastian.timme@liverpool.ac.uk. Member AIAA.

possible for three-dimensional infinite wings [16], while pointing towards imminent instabilities early on where global stability analysis is uninformative.

The method used to achieve triglobal resolvent analysis was of an iterative nature and can be considered a modification of the ideas presented in [17, 18]. Another route, in a fluid flow context, to enable resolvent analysis for more complex test cases was presented in [19], specifically randomized resolvent analysis. In addition to the *conventional* approach, referring to global forcing/response fields, a so-called *spatially windowed* resolvent analysis can be performed [20]. Specifically, the forcing and/or response modes are restricted to a smaller region of the flow (conveniently called a window). Such an analysis has been performed for various flow phenomena, such as jet noise and laminar separation bubble on a two-dimensional aerofoil [21–23]. A windowed resolvent analysis performed on an aerofoil encountering shock buffet investigated the importance of multiple regions in the buffet mechanism [24]. Among other findings, the windowed resolvent method was shown to be capable of recovering non-dominant modes.

The present work will continue the development of the resolvent analysis for practical large aircraft configurations [25], and, in particular, we look into a windowed variant of the method recently implemented in the industry-grade DLR-TAU code [26]. With this in place, we aim to further elucidate the origin of finite-wing shock buffet. In our previous work, the resolvent method was already shown to be a powerful predictive tool in the identification of both modal behaviour well before (in terms of angle of attack) the onset of self-sustained instability and additional modes not accessible through a global stability approach. We continue with a brief description of the theory and implementation details in section II. Focus is on the windowed adaptation of the inexact subspace iterative resolvent algorithm. Results are discussed in section III and conclusions are given in section IV.

II. Theory and Numerical Approach

A. Physical Models

The governing equations, specifically the Reynolds-averaged Navier–Stokes equation, are written in semi-discrete form as

$$\dot{\boldsymbol{w}} = \boldsymbol{R}(\boldsymbol{w}) \tag{1}$$

where $\boldsymbol{w}$ is the state vector and $\boldsymbol{R}$ is the corresponding non-linear residual. Even though the flow model depends on a large number of parameters, these are not explicitly exposed for ease of notation. For the resolvent analysis, the equations undergo a Taylor expansion around a reference state with the fluid unknowns decomposed into a turbulent time-averaged flow and unsteady fluctuation via $\boldsymbol{w}(t) = \bar{\boldsymbol{w}} + \tilde{\boldsymbol{w}}(t)$. Algebraic manipulation results in the equations

$$\dot{\tilde{\boldsymbol{w}}} = J\tilde{\boldsymbol{w}} + \tilde{\boldsymbol{f}} \tag{2}$$

where $J = \partial\boldsymbol{R}/\partial\boldsymbol{w}$ is a large sparse matrix representing the fluid Jacobian matrix. The vector $\tilde{\boldsymbol{f}} = \tilde{\boldsymbol{f}}(t)$ is introduced as a time-dependent forcing, which can be the sum of external forcing and the terms non-linear in $\tilde{\boldsymbol{w}}$.

Using orthogonality, eq. (2) is written at each separate angular frequency ω with $\tilde{\boldsymbol{w}}(t) = \hat{\boldsymbol{w}}e^{i\omega t}$ (and similarly for the forcing vector) such that,

$$i\omega\hat{\boldsymbol{w}} = J\hat{\boldsymbol{w}} + \hat{\boldsymbol{f}} \tag{3}$$

where $\hat{\boldsymbol{w}}$ and $\hat{\boldsymbol{f}}$ are the components of the response and forcing vector, respectively, at frequency ω. Rearranging leads to an input-output relation formulated by the resolvent operator $\mathcal{R}$ as

$$\hat{\boldsymbol{w}} = -\mathcal{R}\hat{\boldsymbol{f}} \tag{4}$$

where $\mathcal{R}$ is explicitly given by $(J - i\omega I)^{-1}$. The resolvent operator can be thought of as transforming an (input) forcing vector $\hat{\boldsymbol{f}}$ into the (output) response state vector $\hat{\boldsymbol{w}}$ and is the focus of resolvent analysis. Resolvent analysis allows investigation of both the optimal forcing/response dynamics at a given frequency and, upon traversing an appropriate frequency range, also for which forcing frequency the largest responses are produced overall, thereby identifying pertinent modal behaviour.

For a given frequency ω, the maximum energy gain of the system, $G(\omega) = \sigma_1^2$, is expressed as

$$G(\omega) = \max_{\hat{f}} \frac{\langle \hat{\boldsymbol{w}}, \hat{\boldsymbol{w}} \rangle}{\langle \hat{\boldsymbol{f}}, \hat{\boldsymbol{f}} \rangle} = \max_{\hat{f}} \frac{\langle \mathcal{R}^{\dagger}\mathcal{R}\hat{\boldsymbol{f}}, \hat{\boldsymbol{f}} \rangle}{\langle \hat{\boldsymbol{f}}, \hat{\boldsymbol{f}} \rangle} \tag{5}$$

where $\langle \boldsymbol{a}, \boldsymbol{b} \rangle = \boldsymbol{a}^H Q \boldsymbol{b}$ defines the weighted inner product of two arbitrary vectors $\boldsymbol{a}$ and $\boldsymbol{b}$, with the matrix Q describing a suitable positive definite matrix. Herein, considering the convenience of the finite-volume spatial discretisation, the

matrix Q contains the discrete cell volumes on its diagonal. Other inner products to represent a suitable energy in the system can be discussed [27, 28]. The adjoint of the resolvent operator is $\mathcal{R}^\dagger$, such that $\langle \boldsymbol{a}, \mathcal{R}\boldsymbol{b} \rangle = \langle \mathcal{R}^\dagger \boldsymbol{a}, \boldsymbol{b} \rangle$, explicitly stated as $\mathcal{R}^\dagger = Q^{-1}\mathcal{R}^H Q = (Q^{-1}J^T Q + i\omega I)^{-1}$. In general, the optimal gain and its corresponding forcing and response modes are obtained by computing the singular value decomposition (SVD), $\mathcal{R} = U\Sigma V^H$, where Σ is a diagonal matrix containing the singular values σ_i (with $\sigma_i \geq \sigma_{i+1}$) and U and V are matrices unitary with respect to Q (so that, for instance, $U^H Q U = I$) [29, 30]. We are interested in the dominant modes of the SVD, having the largest singular values and therefore showing the largest amplification, and a truncated SVD is usually sufficient.

To introduce the windowed resolvent formulation [20, 23], eq. 3 can be rewritten with two window matrices, B and C, augmented by a relation for observable states in the response mode, $\boldsymbol{y}$, such that

$$i\omega\hat{\boldsymbol{w}} = J\hat{\boldsymbol{w}} + B\hat{\boldsymbol{f}} \tag{6a}$$

$$\boldsymbol{y} = C\hat{\boldsymbol{w}}, \tag{6b}$$

This introduces the windowed resolvent operator $\mathcal{H} = C(J - i\omega I)^{-1}B = C\mathcal{R}B$ such that $\boldsymbol{y} = C\hat{\boldsymbol{w}} = -\mathcal{H}\hat{\boldsymbol{f}}$, which is analogous to eq. 4. The same steps can be followed for $\mathcal{H}$ to compute the optimal gain, response and forcing modes via a truncated SVD. The advantage, when compared to a conventional resolvent analysis, is that B and C may be set such that parts of the domain or quantities of interest can be selectively filtered. For instance, when one is interested in a particular flow feature that is far from dominant at a certain frequency, the response or forcing domain can be windowed in such a way that all other, more dominant modes are effectively 'filtered out', such as is demonstrated below. In practice, B and C can be set to be diagonal matrices with unit weights corresponding to locations inside the window (or for selected equations) and zeros to those outside, and identity matrices recover the conventional method.

B. Numerical Methods

Non-linear Solver

The Reynolds-averaged Navier–Stokes equations (plus turbulence model) are solved using the industrial DLR-TAU code which uses a second-order, finite-volume, vertex-centred discretisation [31]. The turbulence closure is provided by the negative Spalart–Allmaras model using the Boussinesq eddy-viscosity assumption. The inviscid fluxes are computed using a central scheme with matrix artificial dissipation. The Green–Gauss theorem is used to compute the gradients of flow variables for viscous fluxes and source terms. The far-field boundary is described as free-stream flow through a characteristic boundary condition while the no-slip adiabatic condition on viscous walls is enforced strongly. A steady-state flow solution is calculated via the backward Euler method with lower-upper symmetric Gauss–Seidel iterations and local time-stepping. A geometric multi-grid method is also used to improve convergence rates.

Inexact Subspace Resolvent Method

Instead of directly computing the SVD of the resolvent operator $\mathcal{H}$ (or the equivalent eigenvalue problems $\mathcal{H}\mathcal{H}^\dagger$ and $\mathcal{H}^\dagger\mathcal{H}$), a novel iterative method is chosen, named the inexact subspace iterative resolvent method. Conventional matrix-forming and/or direct methods are unsuitable due to the size of the linear operators that are required for the test cases of interest. Fortunately, we are interested in computing only a few of the leading modes with the largest energy gains. Therefore, we opt for this novel iterative method to compute the singular values (and corresponding vectors) of the resolvent operator. It is explained in further detail and verified and validated in our companion paper [26]. It replaces the previously used iterative resolvent method for single vectors [25]. The method is summarised in alg. 1. It works by forming two subspace matrices Y_k and F_k to approximate the singular vectors of $\mathcal{H} = B\mathcal{R}C$, in a similar manner to the implicitly restarted Arnoldi method that has previously been used for solving eigenvalue problems [8, 9]. Furthermore, the linear solutions required in lines 6 and 16 of the algorithm do not need to reach a deep level of convergence, hence the method is dubbed *inexact*.

The inexact subspace method involves applying the inverse of a linear operator to a vector, which in practice means the solution of a large sparse linear system of equations using an iterative solver due to the size of the operator. For this purpose, in accordance with the implementation of the triglobal stability tool outlined in [8], we rely on the well established linear harmonic method in the chosen flow solver, adapted for the requirements of the resolvent method. For solving the arising linear systems, we use a Krylov subspace method, in particular the generalised conjugate residual solver with inner orthogonalisation and deflated restarting (GCRO-DR) [32–34] with suitable preconditioning. The GCRO-DR solver aims to improve on the standard restarted generalized minimal residual method by recycling a suitable

Algorithm 1 Windowed inexact subspace iterative resolvent method for k dominant modes

Require: Resolvent operator $\mathcal{H} = C(J - i\omega I)^{-1}B$, convergence criterion tol, required number of modes k and subspace size $m \geq k$

1: Initialise F_m with m random vectors orthogonalised such that $F_m^H B^T Q B F_m = I_m$
2: Initialise $W_m = 0$, $\boldsymbol{\sigma}_m = 0$, $l = 0$
3: **while** $l < k$ **do**
4: **for** $j = l + 1$ to m **do**
5: Set $\boldsymbol{w}_j := \sigma_j \boldsymbol{w}_j$
6: Solve $(J - i\omega I)\Delta\boldsymbol{w} = B\boldsymbol{f}_j - (J - i\omega I)\boldsymbol{w}_j$ inexactly
7: Update $\boldsymbol{w}_j := \boldsymbol{w}_j + \Delta\boldsymbol{w}$
8: Orthogonalise $\boldsymbol{w}_j := \boldsymbol{w}_j - W_{1:j-1}(W_{1:j-1}^H C^T Q C \boldsymbol{w}_j)$
9: Normalise $\boldsymbol{w}_j := \boldsymbol{w}_j / (\boldsymbol{w}_j^H C^T Q C \boldsymbol{w})$
10: **end for**
11: Compute $\Xi = F_{l+1:m}^H Q (J - i\omega I) W_{l+1:m}$
12: Compute SVD of $\Xi = \Psi \Sigma^{\Xi} \Phi^H$ with elements of Σ^{Ξ} arranged in ascending order
13: Update $F_{l+1:m} := F_{l+1:m}\Psi$, $W_{l+1:m} := W_{l+1:m}\Phi$, $\boldsymbol{\sigma}_{l+1:m} = \mathrm{diag}((\Sigma^{\Xi})^{-1})$

14: **for** $j = l + 1$ to m **do**
15: Set $\boldsymbol{f}_j := \sigma_j \boldsymbol{f}_j$
16: Solve $(J^\dagger + i\omega I)\Delta\boldsymbol{f} = C\boldsymbol{w}_j - (J^\dagger + i\omega I)\boldsymbol{f}_j$ inexactly
17: Update $\boldsymbol{f}_j := \boldsymbol{f}_j + \Delta\boldsymbol{f}$
18: Orthogonalise $\boldsymbol{f}_j := \boldsymbol{f}_j - F_{1:j-1}(F_{1:j-1}^H B^T Q B \boldsymbol{f}_j)$
19: Normalise $\boldsymbol{f}_j := \boldsymbol{f}_j / (\boldsymbol{f}_j^H B^T Q B \boldsymbol{f})$
20: **end for**
21: Repeat steps 11-13.

22: **for** $i = l$ to k **do**
23: Compute error norm $\epsilon_i = \max(\|\sigma_i(J - i\omega I)\boldsymbol{w}_i - B\boldsymbol{f}_i\|, \|\sigma_i(J^\dagger + i\omega I)\boldsymbol{f}_i - C\boldsymbol{w}_i\|)$ where $\|\boldsymbol{a}\| = \boldsymbol{a}^H Q \boldsymbol{a}$
24: **if** $\epsilon_i < tol$ **then**
25: Increment number of converged singular triplets $l := l + 1$
26: **end if**
27: **end for**
28: **end while**
29: $Y_k := CW_k$, $F_k := BF_k$

Krylov subspace between restarts (and in principle can also be used to recycle when solving for a sequence of linear systems such as those arising from a changing right-hand side). This helps preventing the algorithm from stalling in particularly stiff cases and normally speeds up convergence. While only the matrix-vector product of the shifted Jacobian operator with an arbitrary vector is needed for the chosen Krylov subspace method, hence a matrix-free method is possible, herein we use an explicitly formed matrix from a hand-derived, analytical formulation. For preconditioning in parallel computing, we use a block-Jacobi-type preconditioner with block-local incomplete lower-upper (ILU) factorisation of either the shifted fluid Jacobian matrix, $(J - i\omega I)$, or its adjoint, $(J^\dagger + i\omega I)$.

III. Results and Discussion

All results are presented in non-dimensional form, using reference length and free-stream reference states (e.g. velocity), unless explicitly stated otherwise.

Cylinder Case

The ubiquitous test case of a circular cylinder at a subcritical Reynolds number has been considered while implementing and verifying the methods discussed in this work. Subcritical laminar circular cylinder flow is discussed

Table 1 Typical parameter settings used for the inexact subspace iterative solver.

Parameter	Value
Maximum number of modes per shift	1
Maximum number of outer iterations	100
Size of subspace for outer iterations	3
Convergence criterion on outer iterations	10^{-5}
Size of Krylov space for inner iterations	120
Number of deflation vectors for inner iterations	20
Convergence criterion on inner iterations	10^{-1}

at a Reynolds number of $Re = 40$ (and low Mach number of $M = 0.2$). A rather coarse mesh with just under 10 000 control volumes was used with the domain extending to a far-field boundary of 100 cylinder diameters, while we observed that the refinement level (despite its coarseness) is sufficient to characterise the pertinent dynamics similar to much finer meshes. The convergence tolerance was set to 10^{-12} throughout both for non-linear iterations of the state-steady computation and the arising linear systems of the efficient unsteady analyses. Stability analysis predicts the leading mode (least damped) with an eigenvalue of $\lambda = -0.0275 + i0.7145$, which eventually develops into the well-known vortex shedding instability at the critical Reynolds number just above $Re = 47$. Overall, results are consistent with published results in the literature [35, 36]. The conventional resolvent analysis was done for an angular frequency $\omega = 0.7$, close to the critical frequency of the Hopf bifurcation at onset condition, and the three leading optimal and sub-optimal modes were computed. The three singular values of those modes without a window present are $\sigma_1 = 2158.98$, $\sigma_2 = 162.66$ and $\sigma_3 = 153.86$. The corresponding leading response and forcing modes can be seen in fig. 2 (top row). The so-called wavemaker can be computed from the direct and adjoint eigenvectors. It is defined at each point i by $\theta_i = \|P_i\hat{\boldsymbol{v}}\|_2 \cdot \|P_i\hat{\boldsymbol{u}}\|_2 / |\langle\hat{\boldsymbol{u}}, \hat{\boldsymbol{v}}\rangle|$, where P_i is a diagonal matrix to extract the relevant variables of the direct ($\hat{\boldsymbol{u}}$) and adjoint vectors ($\hat{\boldsymbol{v}}$) at a given location i describing a discrete control volume. The wavemaker can be seen as the spatial overlap between the two or, alternatively, as the sensitivity of the dynamics to localised feedback [35]. Similarly in the resolvent case (defined with the response and forcing vectors in place of the direct and adjoint vectors), it can be thought of as giving the spatial distribution of the rate of work done by the forcing onto the response mode. Hence, it can therefore indicate where the potential for self-excitation in the flow lies. The wavemaker region (based on stability analysis) is shown in fig. 1 in agreement with literature [35, 37]. This region was shown to be similar to flow stabilisation regions around a cylinder that were found experimentally [38].

For the cylinder case, three different windows are considered for demonstration purposes. The first restricts the response mode to the upper-half plane and the second permits harmonic forcing within the region where (arbitrarily) the wavemaker values are larger than 0.3. The third restricts the forcing to a circle of radius 5, centred on $(x, z) = (40, 0)$, with the aim to not force the wake mode. These results are visualised in fig. 2. In all three cases, the subspace resolvent method was run with the settings summarised in table 1. For the first scenario (response restricted to the upper-half plane only), the forcing and response modes are shown in the second row of the figure. The forcing mode exhibits a strong resemblance to the global forcing mode, shown e.g. in [25, 37]. The response mode is likewise similar to the non-windowed variant, albeit that the lower-half plane gives, of course, exactly zero amplitudes. The gain for this case is $\sigma_1 = 1592.2$, which, interestingly, is almost exactly the gain of the non-windowed case, divided by $\sqrt{2}$, and this can be shown to be true algebraically. For the second scenario (forcing in the wavemaker region), the forcing and response modes are shown in the third row of the figure. Again, the response mode presents a strong resemblance to the non-windowed response mode (albeit with a spatial phase shift, which has not been corrected for the visualisation herein). The forcing mode reveals the pertinent features of the non-windowed forcing mode (noting the spatial phase shift) within the defined window. The optimal gain is $\sigma_1 = 675.4$, demonstrating that even a small region of forcing, if chosen correctly, can still result in significant energy amplification in the system dynamics. Furthermore, it validates the wavemaker as a region in which a high potential for self-excitation lies. In the last scenario, shown in the bottom row of fig. 2, the forcing window is placed far enough downstream of the cylinder that the wake mode is not excited. Indeed, the optimal gain is only $\sigma_1 = 35.6$.

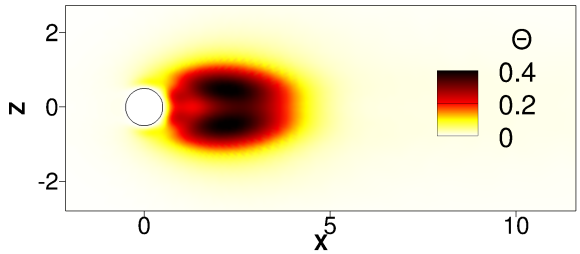

Fig. 1 Wavemaker region for the cylinder.

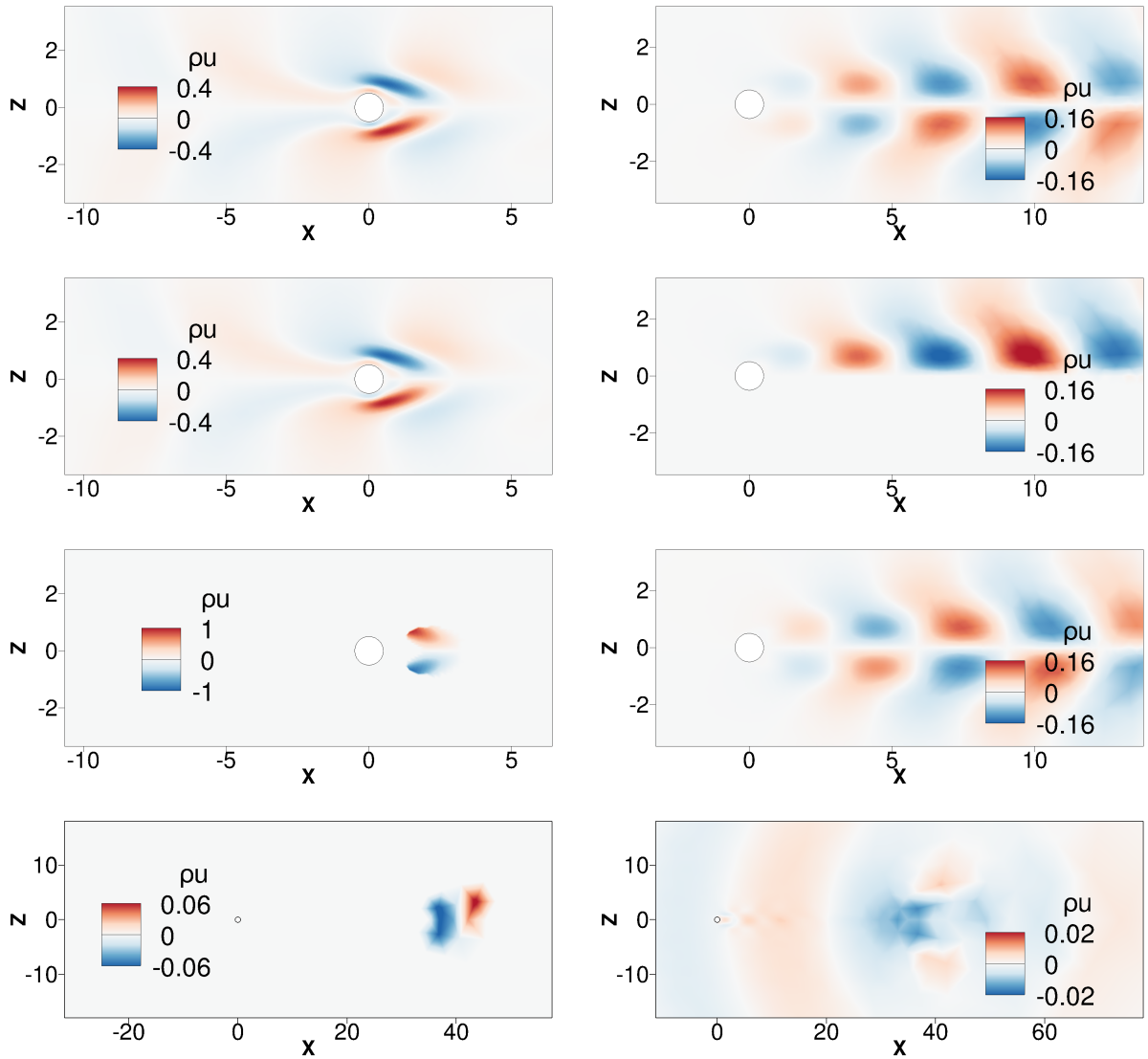

Fig. 2 Real part of the unsteady x-momentum $\widehat{\rho u}$ for (left) forcing and (right) response modes for the cylinder case at angular frequency $\omega = 0.7$. The windows used are (top) none i.e. full domain, (middle top) upper-half plane for the reponse mode, (middle bottom) the region for which the wavemaker is larger than 0.3 and (bottom) a circle far away from the cylinder for the forcing mode.

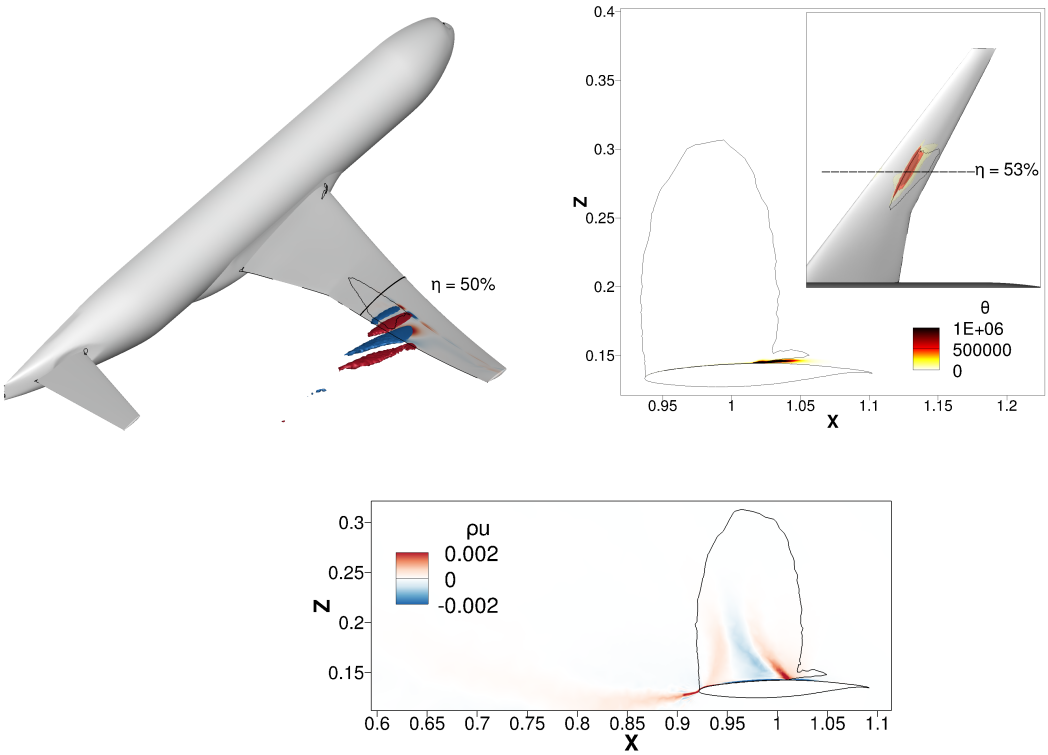

Fig. 3 Buffet mode at angle of attack $\alpha = 3.5°$ showing real part of x-momentum component $\widehat{\rho u}$ for (top left) response as volumetric iso-contours at ±1.5, (top right) momentum-only resolvent wavemaker, and (bottom) forcing at non-dimensional span $\eta = 0.5$. Inset of wavemaker plot shows three iso-surfaces at value $\theta = 1 \times 10^5$, 5×10^5 and 1×10^6. The sonic and zero-skin-friction lines are also shown.

NASA Common Research Model

The NASA Common Research Model (CRM) resembles a modern passenger aeroplane and exists as both a physical model (for wind tunnel testing) and a computational model. It was designed as an open-source test case for the community to explore and compare new ideas and results [39]. The test case is identical to our previous work [8, 9, 25]. The wing has a nominal lift coefficient of 0.5, an aspect ratio of 9, a taper ratio of 0.275 and a 35° quarter-chord sweep angle. Herein, the scaled-down wind tunnel wing/body/horizontal-tail version is discussed featuring a mean aerodynamic chord of 0.189 m with a full span of 1.586 m and reference area of 0.280 m^2. The pylons and nacelles were discarded and the tail-setting angle was 0°. The baseline computational mesh was generated for the half-span configuration with approximately 6.2×10^6 points including approximately 170 000 points on solid walls. A viscous wall normal spacing of $y^+ < 1$ is ensured. The hemispherical far-field boundary is located at a distance of 100 semi-span lengths. Herein, the Reynolds number (based on mean aerodynamic chord) is $Re = 5.0 \times 10^6$ and the free-stream Mach number is $M = 0.85$, chosen according to the test entry in the European Transonic Windtunnel [40]. The focus is on angle of attack $\alpha = 3.5°$ giving subcritical (with respect to the transonic buffet instability) flow conditions. When discussing pseudo-resonances in the resolvent results, awareness of weakly damped eigenmodes in the system dynamics is beneficial, as those can give rise to resonances. These were previously presented in [8]. Most importantly, it was found that there are no weakly damped eigenmodes present at angles of attack $\alpha \leq 3.5°$ that are distinguishable from the majority of spurious fluid modes. Eventually at angle of attack $\alpha \approx 3.7°$, an unstable global mode can be identified at a frequency $\omega \approx 2.5$, linked to shock-buffet dynamics on the wing.

Previously, a conventional resolvent analysis study has been performed for this test case around shock buffet conditions [1, 25]. Specifically, four angles of attack were considered, $\alpha = 3.0°$, 3.25° and 3.5° (below onset) and 3.75° (just above onset). Therein, the single-vector iterative resolvent method was also scrutinised comprehensively, using results on a small test case obtained from a Matlab implementation. The leading singular values from the conventional

resolvent analysis show an angle-of-attack influence. While there is no strong peak to be found in the singular values at angles well below the critical value, the development of pronounced amplification due to optimal forcing tells the potential of the resolvent method as a predictive tool. As said earlier, for angles of attack $\alpha \leq 3.5°$, no weakly damped fluid modes can be found with the stability tool. Developing peaks in the energy gain can hence be explained by an increasing degree of non-normality in the system indicating pseudo-resonance. An increased angle of attack just above buffet onset at $\alpha = 3.75°$ results in a significant increase in energy gain, which has also been found in the two-dimensional aerofoil study in [15]. At this slightly supercritical angle of attack, the peak position in the gain has shifted from approximately $\omega = 5.0$ to a lower value of $\omega = 2.5$, which corresponds to the frequency of the leading fluid mode seen in the eigenspectrum [8]. Additionally, it was shown that including fluid-structure interaction did not have a significant impact on the results of the resolvent analysis. (Pseudo-) resonance with respect to modes that originate in the structural domain was negligible when compared to the non-normality of the fluid Jacobian operator. The optimal response and forcing modes at $\omega = 3.33$ are presented in fig. 3. The response mode shows a strong similarity to the global shock buffet instability mode, with characteristic buffet cells aft of the shock front and outboard-running/downstream features inclined to the trailing edge. Similarly, the forcing mode reveals a resemblance to the corresponding adjoint global mode. The most prominent feature is the oblique line impinging on the shock-foot. It has been shown that this line coincides with a so-called 'characteristic line' and therefore is likely important to the buffet dynamics [15]. Additionally, the so-called resolvent wavemaker, calculated for the wing buffet dynamics [1], is included in the figure (top right). Similar to the wavemaker from an eigenvalue analysis, it gives the 'overlap' of response and forcing modes and shows from where the instability in a system can originate. Specifically, the (resolvent) wavemaker highlights the shock foot and immediate downstream separation region. It is therefore expected that the core of the buffet instability is here. Hence, this region was chosen as one of the windows for the forcing field discussed below.

Next, the windowed resolvent method was run with six different windows for the forcing using the settings in table 1 and the angle of attack is $\alpha = 3.50°$. These regions are visualised in fig. 4. The first was the $M > 1$ supersonic region. The second window is the region for which the resolvent wavemaker (calculated for $\alpha = 3.5°$ and $\omega = 3.33$) was larger than 10^6. The third and fourth are box-shaped windows around the wingtip and inboard (near the wing root), respectively. These windows are chosen so as to not excite the dominant shock buffet mode, but instead less prevalent features with substantially lower gain. For instance, the wingtip vortex mode would only be found at frequencies that are an order of magnitude higher than the buffet mode [1]. The fifth window was defined by all points that lie inside a box-shaped region roughly describing the projection of the wavemaker onto the wing surface. The sixth is a region behind the shock in the middle of the wing and underneath the supersonic zone in front of the shock, so as to exclude the supersonic zone within which the optimal non-windowed mode is mostly situated. It is designed to be similar in function to 'zone 6' in [11], which defined a region behind the shock and above the aerofoil. Therein, it was shown that, for aerofoil shock buffet, it was not possible to suppress the unsteadiness using local selective frequency damping in that region.

Figure 5 summarises the calculated gains for these windows at multiple forcing frequencies. Some interesting observations can be stated. First, for the supersonic-zone region, shown in fig. 4 (top left) and labelled 'Mach' in fig. 5, the gain shows a broad peak and is very close in magnitude to the non-windowed case, peaking at $\omega = 5.0$ with approximately $\sigma_1 = 7.0 \times 10^6$. This can be expected, since the optimal non-windowed forcing mode lies almost entirely within this supersonic region. The optimal forcing mode is not visualised herein for brevity, as it is near identical to the non-windowed forcing mode, shown in fig. 3. The optimal response is identical to the naked eye to the non-windowed response mode, too, and it is therefore not repeated herein either. Next, the 'wavemaker' window, shown in fig. 4 (top right), is discussed. The gains show a similar broad peak behaviour to the non-windowed and supersonic-zone windowed resolvent analysis, indicating the buffet response is excited, as expected. Although this region consists of only roughly 1700 points, i.e. less than 0.1% of the total number of control volumes and roughly 10^{-10}% of the total volume of the computational domain, the gain is approximately $\sigma_1 = 3.4 \times 10^6$ at $\omega = 5.0$, roughly half of the gain computed with the supersonic forcing zone. Like with the cylinder case discussed earlier, despite only forcing a small part of the flow field, the gain is nonetheless a large fraction of the total optimal gain at this frequency. Figure 6 (top left) visualises the corresponding forcing mode at $\omega = 5.0$ for the wavemaker forcing window. The forcing mode shows periodic features along the span, although they are present further upstream than in the response mode. These observations reinforce that the wavemaker region, encompassing the shock foot and separation region, is indeed likely at the core of the buffet phenomenon. Similarly, if the flow in this region could somehow be controlled (cf. the small control cylinder in the cylinder flow case in [38]), shock buffet might be suppressed.

The wingtip and inboard zones, visualised in the middle row of fig. 4, were devised to prevent the dominant buffet response mode from emerging. While the response and forcing modes for the wingtip zone are not shown herein, the wingtip vortex mode is indeed successfully recovered, showing a strong resemblance to the wingtip vortex mode found

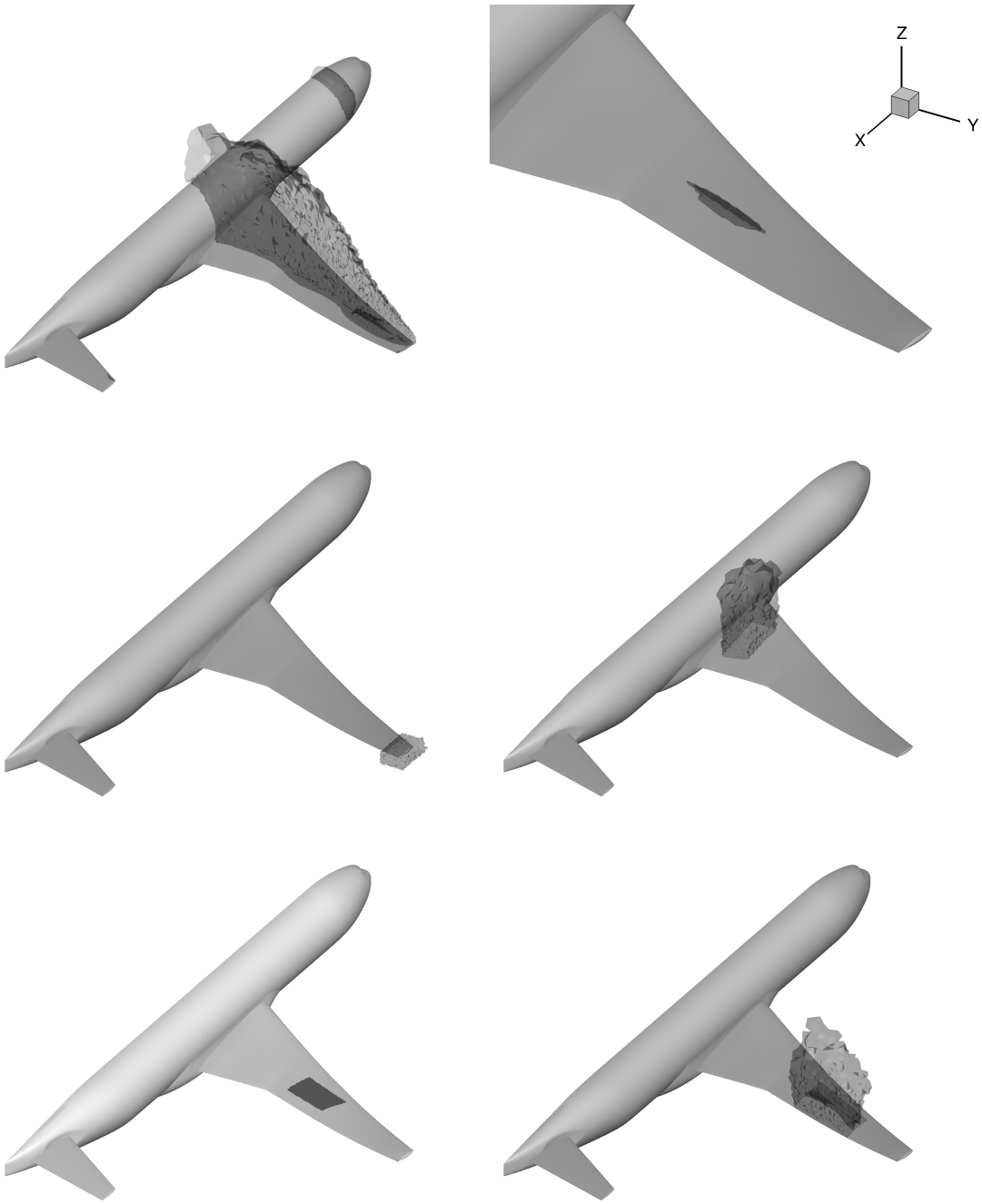

Fig. 4 Visualisation of windowing regions showing zones for (top left) sonic surface, (top right) wavemaker, (middle left) wingtip and (middle right) inboard, (bottom left) surface and (bottom right) behind the shock.

with a conventional resolvent analysis at $\omega \approx 50$, albeit with a longer wavelength, due to the lower forcing frequency herein [1]. The gain is approximately $\sigma_1 = 4 \times 10^3$ at $\omega = 5.0$, and no clear peak is present between $\omega = 3.0$ and 7.0, in contrast to the other windows. It is also interesting to note that the gain is similar in magnitude to the non-windowed gain at $\omega = 51.8$, where it is the dominant mode. Hence, the wingtip mode is likely not sensitive to forcing frequency. These results show that a windowed resolvent analysis can filter out selected flow physics and highlight other phenomena besides the most dominant ones, even if those phenomena would usually not be identified by a conventional resolvent analysis. Hence, a windowed resolvent analysis could be useful in identifying, analysing or preventing flow features that are otherwise not discernible at certain forcing frequencies. The inboard zone, on the other hand, for which the forcing

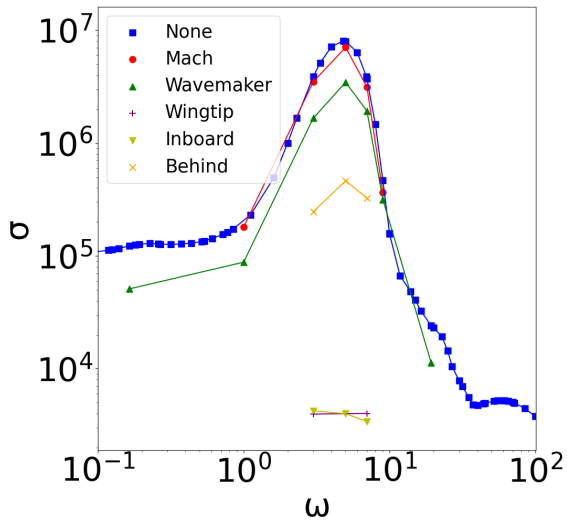

Fig. 5 Leading singular values σ_1 for multiple windowing regions at $\alpha = 3.5°$. The gains for the surface-zone (fifth) window fall outside (below) the plotting range and are therefore not visualised.

and response modes are visualised in fig. 6 (bottom left and right, respectively), did also not result in a buffet-like response mode. Instead, the response mode shows two distinct features. The first is a wake-like structure originating in the inboard zone, in the direction of travel. The second, however, is reminiscent of the inclined shock buffet features aft of the wing, seen in fig. 3, although seemingly less dominant here with a gain of approximately $\sigma_1 = 4.1 \times 10^3$. Such a mode was not found with the conventional resolvent analysis. Indeed, due to the low gain, it is unlikely that such a mode would be found with a conventional analysis that prioritises dominant energy gains.

The surface-zone window, shown in the bottom-left of fig. 4, is defined to represent a zone that could realistically influence the flow in a real-life scenario, for instance by actuators on the surface of the wing [22]. The response mode, not visualised herein, is again the shock buffet mode. The forcing mode (not shown herein either) is similar to that of the wavemaker-zone, visualised in fig. 6, although only present on the surface. However, the gain is very low compared to the non-windowed case (approximately $\sigma_1 = 230$ at $\omega = 3.0$ and $\sigma_1 = 549$ at $\omega = 5.0$, and hence not visible in fig. 5), indicating that there is likely not much potential to control shock buffet. From a numerical point of view, the no-slip boundary condition, enforced strongly at the wing surface, might be a contributing factor, as the momentum equations are effectively not forced for the vertices at the surface.

For the region behind the shock and underneath the supersonic zone, visualised in the bottom right of fig. 4 and denoted in fig. 5 by 'Behind', the optimal gain is an order of magnitude lower when compared to the non-windowed system, despite recovering the shock buffet response mode. The forcing mode, shown in fig. 6 (top right), is concentrated near the boundary layer, both forward and aft of the shock, and is notably absent away from the surface. It seems that this region, especially behind the shock, is not at the core of the shock buffet, but rather contributes to the dynamics, similar to the discussion for the two-dimensional case in [11].

IV. Conclusion

A practical resolvent analysis has previously been accomplished for an industry-relevant aircraft configuration, specifically the NASA CRM [25]. This enables the identification of the optimal forcing and response modes in the entire computational domain together with the energy gain. The windowed, inexact subspace iterative resolvent algorithm, further scrutinised in our companion paper [26], makes it possible to restrict the forcing and response fields (either locally or through selected equations) and is presented herein. This method is verified for a two-dimensional cylinder case, using either the half-plane or wavemaker region as windows for the response and forcing, respectively. For the NASA Common Research Model, we restrict the forcing to selected localised flow regions, including, amongst others, the wavemaker encompassing the shock foot and separated boundary layer, the supersonic region and the wingtip. Using such as a spatially windowed resolvent analysis, we are able to identify the active regions of the shock-buffet dynamics on the finite wing, similar to the previous aerofoil work in [11, 24]. The wavemaker zone reinforces the wavemaker as

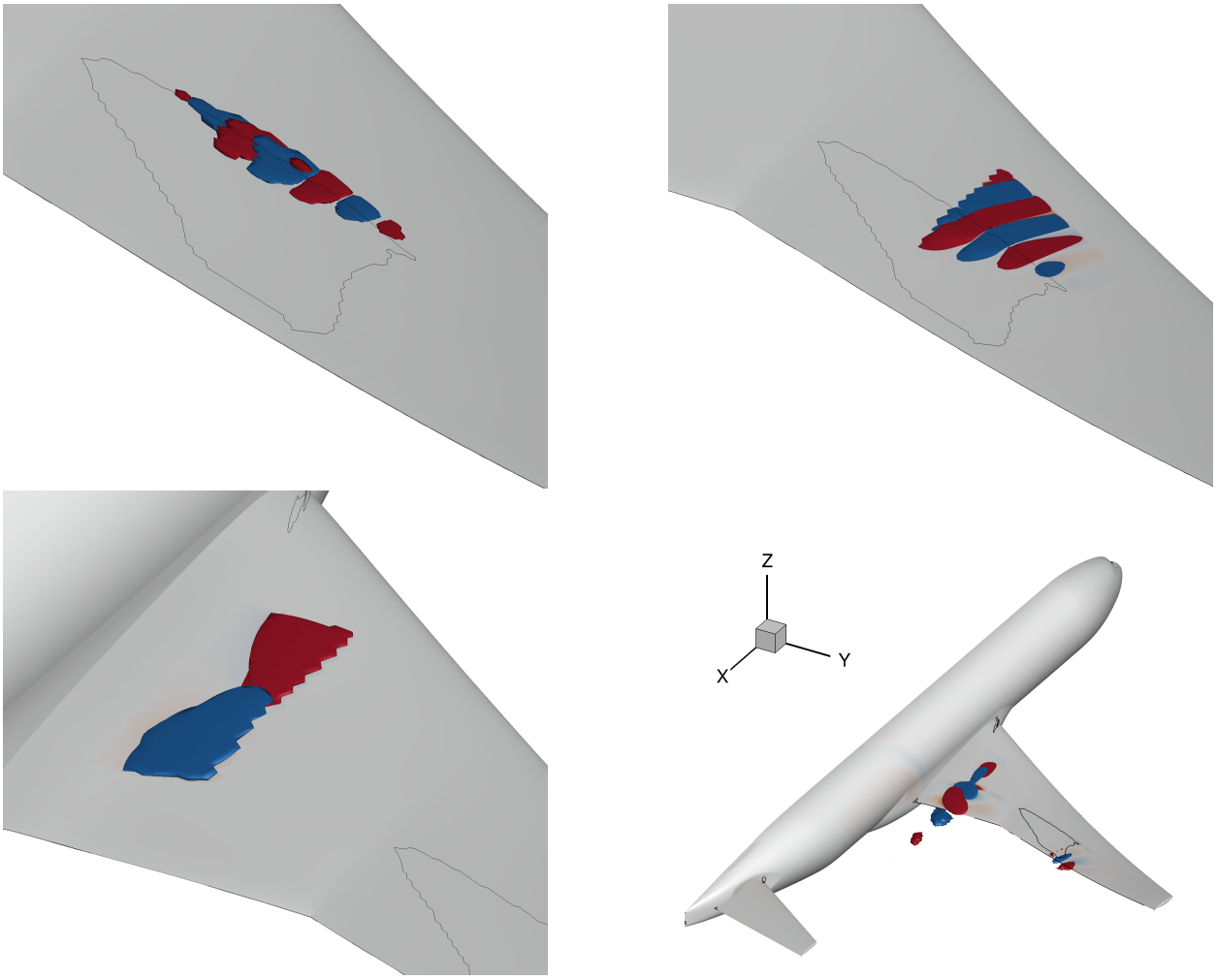

Fig. 6 Visualisation of dominant forcing modes calculated using (top left) wavemaker window, (top right) 'behind the shock' window and (bottom left) inboard window. The dominant response mode for the inboard forcing window is shown bottom right. The volumetric iso-contours are the real part of the x-momentum component $\widehat{\rho u}$ at values of ±0.01 and ±1.5 for forcing and response modes, respectively. The base flow zero skin-friction line is also shown on the surface for orientation.

the core of the instability, whilst selecting a window on the wing surface roughly where the buffet instability emanates results in little energy amplification suggesting limited capability for flow control (but this requires more investigation). Furthermore, it was shown that the windowed resolvent method can filter out unwanted flow features and investigate modes that would otherwise not be found with a conventional global resolvent method. Lastly, windowing the region behind the shock showed that this region is less important to the three-dimensional shock buffet phenomenon, similar to what has been shown for aerofoils. Hence, we contribute to the question on the physical mechanism of finite-wing shock buffet and, through matching a suitable forcing window to practical constraints for flow control on a real wing, on the ability to guide the active/passive control of the phenomenon for future wing design.

Acknowledgments

The first author is grateful for the financial support by an Engineering and Physical Sciences Research Council (EPSRC) Industrial CASE scholarship in partnership with Airbus. We also acknowledge the funding received through the UK project Development of Advanced Wing Solutions (DAWS). The DAWS project is supported by the Aerospace Technology Institute (ATI) Programme, a joint government and industry investment to maintain and grow the UK's

competitive position in civil aerospace design and manufacture. The programme, delivered through a partnership between ATI, Department for Business, Energy & Industrial Strategy (BEIS) and Innovate UK, addresses technology, capability and supply chain challenges. We thank the University of Liverpool for computing time on the high-performance computer and the German Aerospace Center (DLR) for access to the TAU flow solver.

References

[1] Houtman, J., Timme, S., and Sharma, A., "Resolvent analysis of a finite wing in transonic flow," *Flow*, 2023. https://doi.org/10.1017/flo.2023.8, accepted for publication.

[2] Lee, B. H. K., "Oscillatory shock motion caused by transonic shock boundary-layer interaction," *AIAA Journal*, Vol. 28, No. 5, 1990, pp. 942–944. https://doi.org/10.2514/3.25144.

[3] Crouch, J. D., Garbaruk, A., Magidov, D., and Travin, A., "Origin of transonic buffet on aerofoils," *Journal of Fluid Mechanics*, Vol. 628, 2009, p. 357–369. https://doi.org/10.1017/S0022112009006673.

[4] Paladini, E., Beneddine, S., Dandois, J., Sipp, D., and Robinet, J.-C., "Transonic buffet instability: From two-dimensional airfoils to three-dimensional swept wings," *Physical Review Fluids*, Vol. 4, 2019, p. 103906. https://doi.org/10.1103/PhysRevFluids.4.103906.

[5] Crouch, J. D., Garbaruk, A., and Strelets, M., "Global instability in the onset of transonic-wing buffet," *Journal of Fluid Mechanics*, Vol. 881, 2019, p. 3–22. https://doi.org/10.1017/jfm.2019.748.

[6] He, W., and Timme, S., "Triglobal infinite-wing shock-buffet study," *Journal of Fluid Mechanics*, Vol. 925, 2021, p. A27. https://doi.org/10.1017/jfm.2021.678.

[7] Timme, S., and Thormann, R., "Towards three-dimensional global stability analysis of transonic shock buffet," *AIAA Atmospheric Flight Mechanics Conference*, 2016. https://doi.org/10.2514/6.2016-3848, AIAA 2016-3848.

[8] Timme, S., "Global instability of wing shock-buffet onset," *Journal of Fluid Mechanics*, Vol. 885, 2020, p. A37. https://doi.org/10.1017/jfm.2019.1001.

[9] Houtman, J., and Timme, S., "Towards Global Stability Analysis of Flexible Aircraft in Edge-of-the-Envelope Flow," *AIAA SciTech 2021 Forum*, 2021. https://doi.org/10.2514/6.2021-0610, AIAA 2021-0610.

[10] Belesiotis-Kataras, P., and Timme, S., "Aeroelastic Coupling Effects in Globally Unstable Transonic Wing Flow," *AIAA SciTech 2021 Forum*, 2021. https://doi.org/10.2514/6.2021-0611.

[11] Paladini, E., Marquet, O., Sipp, D., Robinet, J.-C., and Dandois, J., "Various approaches to determine active regions in an unstable global mode: application to transonic buffet," *Journal of Fluid Mechanics*, Vol. 881, 2019, p. 617–647. https://doi.org/10.1017/jfm.2019.761.

[12] Trefethen, L. N., Trefethen, A. E., Reddy, S. C., and Driscoll, T. A., "Hydrodynamic Stability Without Eigenvalues," *Science*, Vol. 261, No. 5121, 1993, pp. 578–584. https://doi.org/10.1126/science.261.5121.578.

[13] Jovanovic, M., and Bamieh, B., "Componentwise Energy Amplification in Channel Flows," *Journal of Fluid Mechanics*, Vol. 534, 2005, pp. 145–183. https://doi.org/10.1017/S0022112005004295.

[14] McKeon, B. J., and Sharma, A. S., "A critical-layer framework for turbulent pipe flow," *Journal of Fluid Mechanics*, Vol. 658, 2010, p. 336–382. https://doi.org/10.1017/S002211201000176X.

[15] Sartor, F., Mettot, C., and Sipp, D., "Stability, receptivity, and sensitivity analyses of buffeting transonic flow over a profile," *AIAA Journal*, Vol. 53, No. 7, 2015, pp. 1980–1993. https://doi.org/10.2514/1.J053588.

[16] He, W., and Timme, S., "Resolvent Analysis of Shock Buffet on Infinite Wings," *AIAA Aviation 2020 Forum*, 2020. https://doi.org/10.2514/6.2020-2727.

[17] Monokrousos, A., Åkervik, E., Brandt, L., and Henningson, D. S., "Global three-dimensional optimal disturbances in the Blasius boundary-layer flow using time-steppers," *Journal of Fluid Mechanics*, Vol. 650, 2010, pp. 181—-214. https://doi.org/10.1017/S0022112009993703.

[18] Gómez, F., Sharma, A. S., and Blackburn, H. M., "Estimation of unsteady aerodynamic forces using pointwise velocity data," *Journal of Fluid Mechanics*, Vol. 804, 2016, p. R4. https://doi.org/10.1017/jfm.2016.546.

[19] Ribeiro, J. H. M., Yeh, C.-A., and Taira, K., "Randomized resolvent analysis," *Phys. Rev. Fluids*, Vol. 5, 2020, p. 033902. https://doi.org/10.1103/PhysRevFluids.5.033902.

[20] Schmid, P. J., and Brandt, L., "Analysis of fluid systems: Stability, receptivity, sensitivitylecture notes from the flow-nordita summer school on advanced instability methods for complex flows, stockholm, sweden, 2013," *Applied Mechanics Reviews*, Vol. 66, No. 2, 2014. https://doi.org/https://doi.org/10.1115/1.4026375.

[21] Jeun, J., Nichols, J. W., and Jovanović, M. R., "Input-output analysis of high-speed axisymmetric isothermal jet noise," *Physics of Fluids*, Vol. 28, No. 4, 2016, p. 047101. https://doi.org/10.1063/1.4946886.

[22] Yeh, C.-A., Benton, S. I., Taira, K., and Garmann, D. J., "Resolvent analysis of an airfoil laminar separation bubble at Re=500,000," *Physical Review Fluids*, Vol. 5, No. 8, 2020, p. 083906. https://doi.org/https://doi.org/10.1103/PhysRevFluids.5.083906.

[23] Skene, C. S., Yeh, C.-A., Schmid, P. J., and Taira, K., "Sparsifying the resolvent forcing mode via gradient-based optimisation," *Journal of Fluid Mechanics*, Vol. 944, 2022, p. A52. https://doi.org/10.1017/jfm.2022.519.

[24] Kojima, Y., Yeh, C.-A., Taira, K., and Kameda, M., "Resolvent analysis on the origin of two-dimensional transonic buffet," *Journal of Fluid Mechanics*, Vol. 885, 2020, p. R1. https://doi.org/10.1017/jfm.2019.992.

[25] Houtman, J., Timme, S., and Sharma, A., "Resolvent Analysis of Large Aircraft Wings in Edge-of-the-Envelope Transonic Flow," *AIAA SciTech 2022 Forum*, 2022. https://doi.org/10.2514/6.2022-1329, AIAA 2022-1329.

[26] U S Vevek, and Timme, S., "Resolvent Analysis using Subspace Algorithms for Aerodynamic Applications," *AIAA Aviation 2023 Forum*, 2023. AIAA 2023-xxxx.

[27] Yeh, C.-A., and Taira, K., "Resolvent-analysis-based design of airfoil separation control," *Journal of Fluid Mechanics*, Vol. 867, 2019, p. 572–610. https://doi.org/10.1017/jfm.2019.163.

[28] Bonne, N., Brion, V., Garnier, E., Bur, R., Molton, P., Sipp, D., and Jacquin, L., "Analysis of the two-dimensional dynamics of a Mach 1.6 shock wave/transitional boundary layer interaction using a RANS based resolvent approach," *Journal of Fluid Mechanics*, Vol. 862, 2019, p. 1166–1202. https://doi.org/10.1017/jfm.2018.932.

[29] Trefethen, L. N., and Bau III, D., *Numerical linear algebra*, Vol. 50, Siam, 1997.

[30] Young, N., *An introduction to Hilbert space*, Cambridge university press, 1988. https://doi.org/https://doi.org/10.1017/CBO9781139172011.

[31] Schwamborn, D., Gerhold, T., and Heinrich, R., "The DLR TAU-code: Recent applications in research and industry," *ECCOMAS CFD 2006: Proceedings of the European Conference on Computational Fluid Dynamics*, 2006.

[32] Parks, M. L., de Sturler, E., Mackey, G., Johnson, D. D., and Maiti, S., "Recycling Krylov Subspaces for Sequences of Linear Systems," *SIAM Journal on Scientific Computing*, Vol. 28, No. 5, 2006, pp. 1651–1674. https://doi.org/10.1137/040607277.

[33] Niu, Q., Lu, L.-Z., and Liu, G., "Accelerated GCRO-DR method for solving sequences of systems of linear equations," *Journal of Computational and Applied Mathematics*, Vol. 253, 2013, pp. 131 – 141. https://doi.org/https://doi.org/10.1016/j.cam.2013.04.013.

[34] Xu, S., and Timme, S., "Robust and efficient adjoint solver for complex flow conditions," *Computers & Fluids*, Vol. 148, 2017, pp. 26 – 38. https://doi.org/10.1016/j.compfluid.2017.02.012.

[35] Giannetti, F., and Luchini, P., "Structural sensitivity of the first instability of the cylinder wake," *Journal of Fluid Mechanics*, Vol. 581, 2007, p. 167–197. https://doi.org/10.1017/S0022112007005654.

[36] Sipp, D., and Lebedev, A., "Global stability of base and mean flows: a general approach and its applications to cylinder and open cavity flows," *Journal of Fluid Mechanics*, Vol. 593, 2007, p. 333–358. https://doi.org/10.1017/S0022112007008907.

[37] Symon, S., Rosenberg, K., Dawson, S. T. M., and McKeon, B. J., "Non-normality and classification of amplification mechanisms in stability and resolvent analysis," *Phys. Rev. Fluids*, Vol. 3, 2018, p. 053902. https://doi.org/10.1103/PhysRevFluids.3.053902.

[38] Strykowski, P. J., and Sreenivasan, K. R., "On the formation and suppression of vortex 'shedding' at low Reynolds numbers," *Journal of Fluid Mechanics*, Vol. 218, 1990, p. 71–107. https://doi.org/10.1017/S0022112090000933.

[39] Vassberg, J., Dehaan, M., Rivers, M., and Wahls, R., "Development of a Common Research Model for Applied CFD Validation Studies," *26th AIAA Applied Aerodynamics Conference*, 2008. https://doi.org/10.2514/6.2008-6919.

[40] Lutz, T., Gansel, P. P., Waldmann, A., Zimmermann, D.-M., and Schulte am Hülse, S., "Prediction and Measurement of the Common Research Model Wake at Stall Conditions," *Journal of Aircraft*, Vol. 53, No. 2, 2016, pp. 501–514. https://doi.org/10.2514/1.C033351.